

Discontinuity in the family pattern of single-wall carbon nanotubes

K. Sato,¹ R. Saito,¹ J. Jiang,² G. Dresselhaus,³ and M. S. Dresselhaus⁴

¹Department of Physics, Tohoku University and CREST JST, Sendai, 980-8578, Japan

²Department of Physics, NC State University, Raleigh, North Carolina 27695-7518, USA

³Francis Bitter Magnet Laboratory, Massachusetts Institute of Technology, Cambridge, Massachusetts 02139-4307, USA

⁴Department of Physics, Massachusetts Institute of Technology, Cambridge, Massachusetts 02139-4307, USA

(Received 9 July 2007; revised manuscript received 19 September 2007; published 29 November 2007)

The higher lying bright exciton energies ($E_{11}^M, E_{33}^S, E_{44}^S, E_{22}^M, E_{55}^S, E_{66}^S, E_{33}^M$) of single-wall carbon nanotubes are calculated by solving the Bethe-Salpeter equation within an extended tight binding method. For smaller diameter nanotubes, some higher E_{ii} excitonic states are missing. In particular, some E_{ii} 's on the one-dimensional Brillouin zone (cutting line) are no longer relevant to the formation of excitons and are skipped in listing the order of the E_{ii} values. Thus the family patterns show some discontinuities in k space and this effect should be observable in Raman G' band spectroscopy. The higher exciton energies E_{33}^S and E_{44}^S have a large chirality dependence due to many body effects, since the self-energy becomes larger than the binding energy. Thus the chirality dependence of the higher E_{ii} comes not only from a single particle energy but also from many-body effects.

DOI: 10.1103/PhysRevB.76.195446

PACS number(s): 78.67.Ch, 78.67.-n, 71.35.Cc

I. INTRODUCTION

The exciton physics of single-wall carbon nanotubes (SWNTs) have been investigated significantly for photoluminescence (PL) and resonance Raman spectroscopy (RRS), which gives a rich information for sample characterization and new exotic physics.¹⁻⁸ The optically allowed transition energies of an exciton for parallel polarization to a SWNT axis are denoted by E_{ii} , from lower energy $E_{11}^S, E_{22}^S, E_{11}^M, E_{33}^S, E_{44}^S, E_{22}^M, \dots$,⁹ for a transition between i th conduction (an electron) and i th valence (a hole) energy bands. Originally E_{ii}^S denoted a van Hove singular energy for the joint density of states for the one-particle energy bands of a SWNT.⁹ Here we will use the same notation for the transition energies of the exciton which consists of the electron and the hole wave function in the i th energy subbands.

The occurrence of the E_{ii} energy is understood by the singular joint density of states in which the i th cutting line⁹⁻¹¹ close to the K point (hexagonal corner) in the two-dimensional (2D) Brillouin zone, has an energy minimum (maximum) at k_{ii} for the conduction (valence) bands. Since the electron energy dispersion of 2D graphene is approximated to be linear on k around the K point for a small k ,¹² the order of E_{ii} is thus determined by the distance of the cutting lines from the K point. This situation does not generally change for the exciton E_{ii} in which some k states around the energy minimum (maximum) are mixed to one another to make spatially localized exciton wave function. However, for smaller diameter (d_t) SWNTs, the distance of two cutting lines becomes larger, the trigonal warping effect and the curvature effect might change the order of E_{ii} values from the i th cutting line, which is the subject of the present paper. This phenomena is important especially for the assignment of (n, m) from the family pattern. For higher E_{ii} values, a clear definition of E_{ii} itself is necessary.

In the experiment of PL and RRS, the E_{ii} values as a function of d_t^{-1} give similar energies to one another for the same $2n+m$ of (n, m) SWNTs, which we call the family

pattern.^{13,14} It is important for knowing the family value $2n+m$ in the spectra of PL or RRS, since the family pattern makes the assignment for (n, m) easy. Since a $2n+m = \text{const}$ family has a similar diameter,^{11,12,15} the E_{ii} values within the $2n+m$ family show a unique chiral angle dependence which we call family spread. Depending on $\text{mod}(2n+m, 3) = 1$ or 2 , the $(2n+m)$ families divide into type I and II, semiconductor SWNT family, respectively, while $\text{mod}(2n+m, 3) = 0$ corresponds to the metallic SWNT family. The direction of the family spread is different for types I and II with the same E_{ii}^S from larger (an armchair SWNT) to smaller (a zigzag SWNT) chiral angle. In the case of E_{ii}^M , the joint density of states for a (n, m) SWNT split into two (the higher E_{iiH}^M and lower E_{iiL}^M), and the different direction of the family spread for E_{iiH}^M and E_{iiL}^M are opposite to each other. The origin of the family spread is due to (1) the trigonal warping effect of the electronic energy,⁹ (2) the curvature effect,¹³ and (3) the environmental effect (or many body effect).¹⁶⁻¹⁹

E_{ii} values consist of one-particle energies and many-body corrections which are further decomposed into an exciton binding energy E_{bd} and a self-energy Σ . The one particle energy is calculated by the extended tight binding (ETB) calculation^{12,13,20} in which we consider the curvature effect. The calculated results of the ETB method reproduce well the family behavior, especially for smaller SWNTs. The difference of the observed E_{ii} from the ETB E_{ii} is many body corrections. We showed that the many body correction for E_{11}^S and E_{22}^S is expressed by a logarithmic function²¹ of d_t .²² The family spread for E_{11}^S mainly come from the one particle energy since the family spread for E_{bd} is canceled by that for Σ .

However, the cancellation of E_{bd} and Σ does not work well for higher E_{ii} values. Araujo *et al.* claimed that for E_{33}^S and E_{44}^S and that a universal curve for the many body correction for E_{33}^S and E_{44}^S apparently deviates from that for E_{11}^S and E_{22}^S .^{24,25} The energy shift from the logarithmic function of the many body correction is inversely proportional to the diameter of a SWNT $1/d_t$ showing that the shift is related to the many body effect.

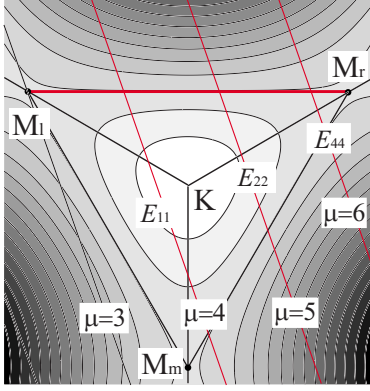


FIG. 1. (Color online) Wave vectors of a (6, 1) nanotube around the K point are shown. The wave vector lines must cross the $M_l M_r$ line segment in order to have an E_{ii} within the $3M$ region.

In a previous paper,²⁶ we showed that E_{33}^S and E_{44}^S are nothing but exciton states too and that the many body effect also affects the family spread.²⁶ Since the self-energy becomes larger than the absolute value of the exciton binding energy with increasing i for E_{ii} , the cancellation of the family spread for the many-body effect does not occur any more for E_{33}^S and E_{44}^S .

Furthermore, we found that the family spreads for E_{33}^S and E_{44}^S overlapped with each other, especially for smaller diameter SWNTs. In this case, the order of E_{ii} as a distance of k from the K point does not exist any more. In this paper, we will investigate this behavior by showing the many body interaction more explicitly and we try to show some verification of this effect by comparing our results to previously reported Raman spectroscopy results. We will also discuss the behavior for E_{22}^M , E_{55}^S , and E_{66}^S .

In Sec. II we show a brief explanation of the cutting line distances and the method for the exciton calculation. In Sec. III we present calculated results for the E_{11}^M , E_{33}^S , E_{44}^S , E_{22}^M , E_{55}^S , and E_{66}^S energies, which are then compared with E_{11}^S and E_{22}^S . In Sec. IV, a summary is given.

II. CONDITION FOR THE CUTTING LINES AND THE CALCULATIONAL METHOD

In the 2D Brillouin zone of graphene, a triangular region which connects three M points around a K (or K') point (see Fig. 1) is important for exciton physics, since the energy dispersion of the conduction (valence) band for a SWNT has a minimum (maximum) only in the triangular region. Hereafter we call this triangle the $3M$ triangle. The remaining region of the Brillouin is a hexagonal region which connects six M points around the Γ point. In the hexagonal region, the conduction (valence) band gives only a maximum (minimum) which also gives a singular joint of density of states but a minimum electron-photon matrix element at the singular point.²⁷ Thus if a cutting line lies outside of the $3M$ triangle, the cutting line does not contribute to the optical absorption at E_{ii} .

For example, we cannot see E_{33} optical absorption for a (6, 1) chiral nanotube as shown in Fig. 1. Here we plot the wave vectors for a (6, 1) chiral nanotube around the K point. Three red color lines denote the wave vectors which can contribute to E_{ii} . Since the (6, 1) nanotube is classified as a type I nanotube, we expect that E_{11} and E_{33} are on the left side from the K point. However the cutting line, which is the third nearest neighbor from the K point, cannot lie within the $3M$ triangle, and therefore E_{33} exists not on the left side but E_{44} exists on the right side of the K point, as shown in Fig. 1. E_{33} is thus skipped. In Sec. III, we show that some E_{ii} values from van Hove singular k_{ii} points change and skip when listing the E_{ii} levels in the order of their energy values. The reason for this situation is the trigonal warping effect of the single-particle electronic energy.⁹ The important fact that the singular point of E_{33} does not exist on the third closest cutting line to the K point is seen in the G' -band Raman spectra around 2700 cm^{-1} since the G' -band frequency depends on the q vector of phonons in a double resonance Raman process.^{28,29}

In the (n, m) assignment it is useful for us to know the maximum E_{ii} transition observed for a given (n, m) SWNT. Here we derive the formulas for how many cutting lines exist within the $3M$ triangle. The coordinates of the three M points around the K point are (see Fig. 1)

$$M_l = \left(\frac{\pi}{\sqrt{3}a}, \frac{\pi}{a} \right), \quad M_m = \left(\frac{2\pi}{\sqrt{3}a}, 0 \right), \quad M_r = \left(\frac{\sqrt{3}\pi}{a}, \frac{\pi}{a} \right), \quad (1)$$

where a is the lattice constant. Here we consider the (n, m) SWNTs with chiral angles in the range $0^\circ \leq \theta \leq 30^\circ$, which corresponds to $0 \leq m \leq n$ in the standard notation.¹² In this case, all cutting lines are in the $3M$ triangle, where θ crosses the $M_l M_r$ line segment on which the number of crossing points correspond to the number of possible E_{ii} values. Here we consider cutting lines with infinite length.

When we defined the cutting lines as the one-dimensional Brillouin zone,¹² the lines are finite with the length $2\pi/T$ (T in the unit vector of a SWNT) in k space. However, if we consider the cutting lines with finite length, the situation is not simple. Thus we consider here a straight line for extending the cutting lines in the direction of the cutting line.

Then a k point on the μ th cutting line for an (n, m) SWNT is expressed by as follows:

$$k = \mu K_1 + t K_2 = \frac{1}{N} [(tm - \mu t_2) \mathbf{b}_1 + (\mu t_1 - tn) \mathbf{b}_2] \equiv (k_x, k_y), \quad (2)$$

where $-\infty < t < \infty$ and μ is taken as the number of the line which we label starting from $\mu=0$ at the Γ point. K_i and \mathbf{b}_i ($i=1, 2$) are, respectively, reciprocal lattice vectors of the SWNT and of 2D graphite as defined by¹²

$$\mathbf{K}_1 = \frac{1}{N} (-t_2 \mathbf{b}_1 + t_1 \mathbf{b}_2), \quad \mathbf{K}_2 = \frac{1}{N} (m \mathbf{b}_1 - n \mathbf{b}_2) \quad (3)$$

and

$$\mathbf{b}_1 = \left(\frac{2\pi}{\sqrt{3}a}, \frac{2\pi}{a} \right), \quad \mathbf{b}_2 = \left(\frac{2\pi}{\sqrt{3}a}, -\frac{2\pi}{a} \right), \quad (4)$$

where integers t_1 and t_2 are defined by

$$t_1 = \frac{2m+n}{d_R}, \quad t_2 = -\frac{2n+m}{d_R}, \quad (5)$$

where

$$d_R = \text{GCD}(2n+m, 2m+n). \quad (6)$$

Here the function of GCD is defined as the greatest common divisor of two integers.¹² From Eq. (2), we get the formulas for (k_x, k_y)

$$k_x = \frac{\beta}{\sqrt{3}}[(m-n)t + 3(m+n)\mu], \quad (7)$$

$$k_y = \beta[(m+n)t - (m-n)\mu], \quad (8)$$

with

$$\beta = \frac{\pi}{(n^2 + m^2 + nm)a}. \quad (9)$$

Then the μ th cutting line is expressed by a linear function of k_x and k_y as follows:

$$(m-n)k_y = \sqrt{3}(n+m)k_x - \frac{4\pi}{a}\mu. \quad (10)$$

In the case of armchair nanotubes ($n=m$), Eq. (10) gives a vertical line in the (k_x, k_y) plane and for the other cases ($n \neq m$), and k_y is given by a function of k_x , $f(k_x)$:

$$m=n: k_x = \frac{4\pi\mu}{\sqrt{3}a(m+n)}, \quad (11)$$

$$m \neq n: f(k_x) = k_y = \sqrt{3} \frac{m+n}{m-n} k_x - \frac{4\pi}{a(m-n)} \mu. \quad (12)$$

Equations (11) and (12) can have a crossing point on the $M_i M_r$ line segment whose condition is given by

$$m=n: \frac{\pi}{\sqrt{3}a} < k_x < \frac{\sqrt{3}\pi}{a}, \quad (13)$$

$$m \neq n: \frac{\pi}{a} < f\left(\frac{\pi}{\sqrt{3}a}\right) \quad \text{and} \quad f\left(\frac{\sqrt{3}\pi}{a}\right) < \frac{\pi}{a}. \quad (14)$$

From Eqs. (13) and (14), we get the conditions for μ ,

$$m=n: n+m < 4\mu < 3(n+m), \quad (15)$$

$$m \neq n: n < 2\mu < 2n+m. \quad (16)$$

Thus the possible number of E_{ii} is less than $(n+m)/2$ for the above two cases. Although this statement is easy to remember, we must check each μ one by one in the real case since we did not consider in the above equations the curvature effect and the many body (exciton) effects of SWNTs.

In the case of Fig. 1, for example, the number of E_{ii} for the (6, 1) nanotube is three, given by Eq. (16)

$$3 < \mu < \frac{13}{2}, \quad \mu = 4, 5, 6. \quad (17)$$

Since the K point for the (6,1) SWNT corresponds to a rational μ value $\mu_K = (2n+m)/3 = 13/3 \sim 4.3$ [see Eq. (4.2) in Ref. 12], we also know that the order of the cutting lines is not regular. In fact, the regular pattern for $\mu_K \sim 4.3$ for E_{11}^S , E_{22}^S , and E_{33}^S would be $\mu = 4, 5$, and 3 (not 6). Thus we can check the irregular order of the cutting lines for all (n, m) values without any difficulty.

The bright exciton energies of SWNTs are calculated by solving the Bethe-Salpeter equation (BSE) in which the one-particle energies are given by the ETB method.²³ The formulation of the BSE is given in a previous paper.²³ We consider the Coulomb interaction only for π electrons for simplicity and we adopt the random phase approximation for a polarization function of the π electrons. The Ohno potential which is widely used for one-dimensional conductors is adopted for describing the Coulomb interaction. As for the surrounding materials of a SWNT, we express this environmental effect on the exciton binding energy by a static dielectric constant κ . Here we used the value of $\kappa = 2.22$ in the calculation which reproduces the experimental values of the Raman E_{ii} or PL E_{ii} for SWNT bundle samples.²³ For the other samples, we need to consider a correction to the environmental effect,¹⁹ which we will not discuss here. In this calculation, we use the same function as Eq. (3.8) in Ref. 30 with a cutoff energy (10 eV) and a parameter of $\alpha = 4$. We have checked that the self-energies for E_{33}^S and E_{44}^S do not change by changing these parameters.

Because of time-reversal and spatial symmetries, any excitons state is an irreducible representation of the symmetry group³¹ and only the A_2 singlet exciton is an optically dipole-allowed state (bright exciton) and the other symmetry excitons are dark excitons. Here we will consider only the bright exciton states since the resonance Raman spectra and the one-photon PL spectra are related to the optical dipole transition of the bright exciton. Further we will discuss only the lowest exciton states for each E_{ii} value and we did not consider here the exciton excited states. In fact, the optical transition matrix element becomes sufficiently small for the excited states, and therefore we will not see the excited exciton states in the Raman excitation profile unless the experimentalists pay special attention to see such an effect.

III. CALCULATED RESULTS AND DISCUSSION

A. Semiconducting SWNTs

Figure 2 shows the calculated results for the bright exciton Kataura plot in the diameter range between 0.3 and 3.0 nm. Red, blue, and black symbols denote type I, type II semiconducting, and metallic nanotubes, respectively. E_{ii} is calculated up to E_{66}^S and E_{33}^M . The integers in Fig. 2 denote $2n+m$ family numbers. If one knows the family number up to E_{11}^M , the same family number for the higher E_{ii} values can be applied for the same diameter and for the same nanotube type.

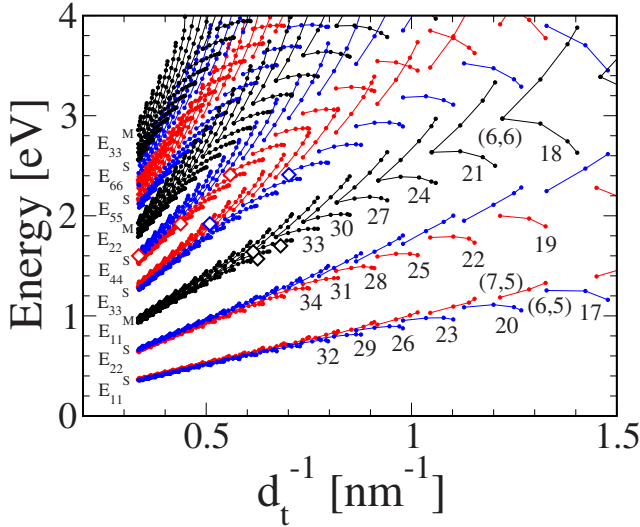


FIG. 2. (Color online) The bright exciton energy Kataura plot as a function of inverse diameter. E_{ii} is up to E_{66}^S and E_{33}^M . Red, blue and black symbols denote type I, type II, and metallic nanotubes, respectively. The eight diamond symbols are experimental data by Sauvajol *et al.* (Ref. 32).

The eight diamond symbols in Fig. 2 are experimental results for suspended SWNTs by Sauvajol *et al.*³² in which they succeeded with an assignment of (n,m) for SWNTs with diameters up to 3 nm using an electron-diffraction technique in their Raman-TEM experimental setup. Even though their results are for isolated suspended SWNTs, and the calculation is for bundles, the calculated results for their assigned (n,m) values reproduce all eight points within the environmental effect shifts (up to 80 meV). Since the results of Sauvajol *et al.*³² are for isolated SWNTs and since we used the κ value (≈ 2.22) in the calculation which is fitted to bundle SWNTs, we expect some shifts in E_{ii} because of the environmental effect. In their previous paper, they compared their measurements with another theoretical calculation which does not consider the excitonic effect, and they then needed to shift their data by about 0.3–0.4 eV from the theoretical calculation for fitting.³² However, the present calculation does not need any shifts. Since the diameter of the experiment is very large (2–3 nm), this environmental effect is much smaller, even though the many body effect cannot be neglected. In order to check our calculation more carefully, more experimental data are highly desired, and such work will contribute to the progress of Raman spectroscopy of SWNTs.

It is clear that so many E_{ii} values for many (n,m) SWNTs are seen for SWNTs with diameters larger than $d_t^{-1} < 0.7$ and for a larger energy region than 2 eV. Thus the assignment of (n,m) for larger diameter SWNTs which can be done by the electron diffraction technique,³² might be difficult only by resonance Raman excitation experiments. However, we know the fact that a zigzag nanotube gives a strong RBM intensity relative to an armchair nanotube for a similar diameter.²³ Thus from the observed family pattern, experimentalists can fit the strongest intensity point in a family pattern to $(n,0)$ or zigzag nanotubes.

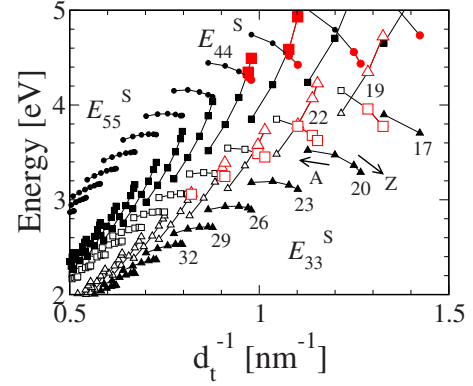


FIG. 3. (Color online) The bright exciton energy Kataura plot for E_{33}^S , E_{44}^S . Open (solid) triangles and squares denote type I (type II) E_{33}^S and E_{44}^S , respectively. Circles denote type II E_{55}^S . Red symbols denote the exchange of the order of cutting lines.

In Fig. 3, we plot the calculated results of the E_{33}^S and E_{44}^S bright exciton energies as a function of inverse diameter. Open (solid) triangles and squares denote type I (type II) E_{33}^S and E_{44}^S , respectively. For smaller diameter type I SWNTs, the E_{33}^S and E_{44}^S lines with the same family number cross each other. This crossing means that the third (fourth) nearest cutting line to the K point gives the fourth (third) exciton energy. Here the higher exciton energy means not the excited exciton states for a given cutting line but the lowest energy exciton states for different cutting lines. If we define E_{ii}^S from the smaller energy states, the family pattern would give a kink at the crossing point in the Kataura plot. Thus it should be natural for us to define the E_{ii}^S on a smooth curve of the family pattern on the i th nearest cutting line. In this case, some E_{ii}^S for some (n,m) might be missing.

In Fig. 3, four red solid squares in E_{44}^S with $2n+m = 23, 26$ are obtained on the cutting line for the fifth closest cutting lines to the K point which generally gives E_{55}^S . Between E_{44}^S and E_{55}^S , the energy region for E_{22}^M exists. It is surprising that the exchange of the family pattern between E_{44}^S and E_{55}^S nevertheless occurs smoothly.

In Fig. 4 we show the extended region of the Kataura plot for E_{55}^S , E_{66}^S , E_{33}^M . When we see the zigzag nanotube region which is the broadened end in the family pattern, the overlap with the other E_{ii} band is significant for large diameter SWNTs. The assignment of E_{ii} and (n,m) should be performed along the family patterns.

B. Metallic SWNTs

In Fig. 5, the calculated results for the E_{11}^M bright exciton states for SWNTs with $0.6 < d_t^{-1} < 1.4 \text{ nm}^{-1}$ are plotted as a function of inverse diameter d_t^{-1} . Solid and open circles denote the higher and lower E_{11}^M values. In the case of armchair SWNTs, the two cutting lines are equivalent to each other and thus no splitting of E_{11}^M occurs.¹²

In Fig. 6, we plot the self-energy Σ and the exciton binding energy E_{bd} for E_{11}^M as a function of d_t^{-1} . Both the lower and the upper E_{11L}^M and E_{11H}^M transition energies show a family pattern for Σ and E_{bd} . The values are largest for zigzag

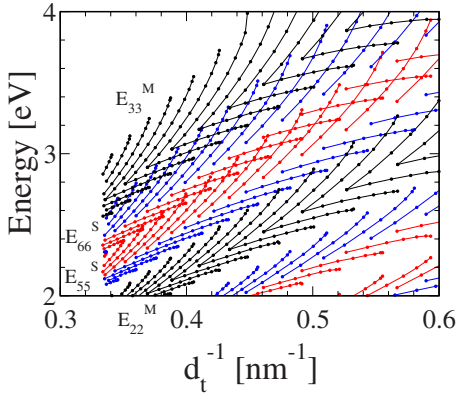


FIG. 4. (Color online) The bright exciton energy Kataura plot for E_{22}^M , E_{55}^S , E_{66}^S , E_{33}^M . Red, blue and black symbols denote type I, type II, and metallic nanotubes, respectively.

nanotubes within a family, because the effective mass is larger and the curvature-induced small energy gap is larger for zigzag nanotubes. However, $\Sigma - E_{\text{bd}}$ in Fig. 6 does not show any chiral angle dependence, but does show a simple diameter dependence. This cancellation for the chiral angle dependence is similar to that found for E_{11}^S and E_{22}^S ,²³ while the diameter dependence does not at all fit well to the logarithmic function (dotted line in Fig. 6) (Refs. 23 and 24)

$$E^{\text{ln}} = 0.55(2p/3d_t)\ln[3/(2p/3d_t)], \quad (18)$$

with $p=3$. The reason for the deviation from the logarithmic function is that E_{bd} for E_{11}^M is much smaller than for E_{11}^S or E_{22}^S because of the screening of free electrons in metallic SWNTs.

It should be mentioned that the fitted logarithmic function [Eq. (1) by Araujo *et al.*²⁵] has different fitting parameters from Eq. (18). The function proposed by Araujo *et al.* is a fitted function to the term after subtracting the chirality dependent, single particle, and many-body terms from the observed E_{ii} values. Thus we can not directly compare our many-body terms as shown in Fig. 6 with their results.

In Fig. 7 we plot the polarization function²³ for π electrons for metallic zigzag SWNTs. The inset is that for semiconducting SWNTs. A small oscillation comes from numerical inaccuracy for the finite system calculations. For semiconducting SWNTs, $\epsilon(0, q)$ has a maximum around q

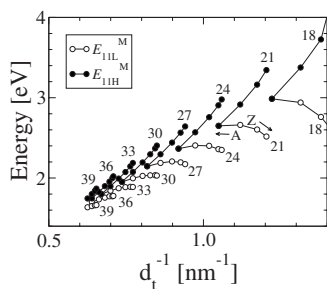


FIG. 5. The E_{11}^M exciton energy Kataura plot. Open and solid symbols denote E_{11L}^M and E_{11H}^M , respectively. The symbols A and Z denote armchair and zigzag SWNTs, respectively.

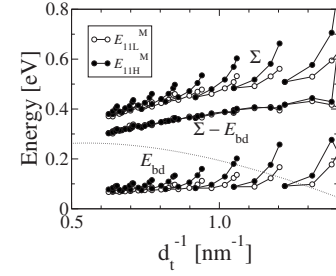


FIG. 6. The self-energy Σ , the binding energy E_{bd} , and the difference energy $\Sigma - E_{\text{bd}}$ for E_{11}^M are plotted as a function of d_t^{-1} . The dashed line is the scaling law with $p=3$. Open and solid symbols denote E_{11L}^M and E_{11H}^M , respectively.

$= 1-2 \text{ nm}^{-1}$, which contributes for the nanotube to the spacial localization around 1 nm. In metallic nanotubes, a Drude-type singularity around $q \sim 0$ is seen in $\epsilon(0, q)$ for (12,0) and (18,0) which results in some screening of E_{bd} especially for long-range Coulomb interactions, while a similar behavior of $\epsilon(0, q)$ to that for semiconducting SWNT can be seen for the (6,0) tube because of a curvature-induced energy gap ($\sim \text{meV}$) which can affect the Coulomb energy. First-principles calculations show that the smallest diameter SWNTs all exhibit metallic behavior³³ because of the lowering of the antibonding σ band and thus we must consider the effect of other electrons for obtaining the exciton energy for such small diameter SWNTs.

C. Many body effect for E_{33} and E_{44}

In Fig. 8, we plot, respectively, $\Sigma - E_{\text{bd}}$ for E_{11}^S , E_{22}^S , E_{33}^S , and E_{44}^S on an expanded energy scale as a function of d_t^{-1} . It is clear from the figure that the chirality dependences of $\Sigma - E_{\text{bd}}$ for E_{33}^S and E_{44}^S are much larger than those for E_{11}^S and E_{22}^S . The reason for the family spread for E_{33}^S and E_{44}^S is that the self-energies for E_{33}^S and E_{44}^S are larger than those for E_{11}^S and E_{22}^S and thus the cancellation between Σ and E_{bd} does not occur.

Another important point is that a family spread can be seen in $\Sigma - E_{\text{bd}}$ for E_{33}^S and E_{44}^S ,²⁶ which is comparable to the family spread observed in the ETB single particle calculations. This means that the origin of the family spread for E_{33}^S

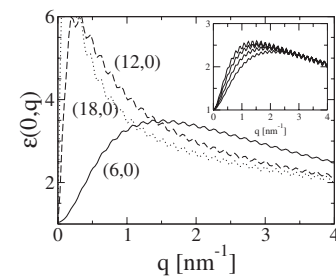


FIG. 7. The polarization function $\epsilon(0, q)$ of metallic zigzag nanotubes for (6,0), (12,0) and (18,0). The inset shows $\epsilon(0, q)$ of semiconducting zigzag nanotubes (10,0), (13,0), (16,0), and (19,0) from the bottom as a function of q .

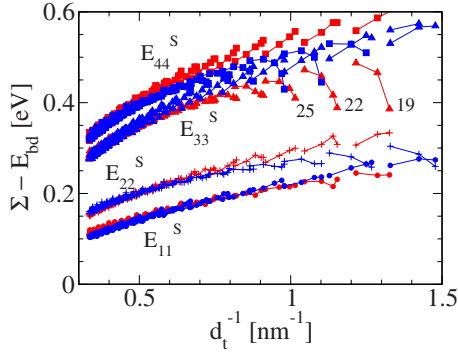


FIG. 8. (Color online) $\Sigma - E_{\text{bd}}$ of $E_{ii}^S (i=1,2,3,4)$ is plotted as a function of d_t^{-1} . The red (blue) symbols denote semiconducting type I (type II) SWNTs, in which circles, pluses, triangles and squares are for E_{11}^S (circles), E_{22}^S (pluses), E_{33}^S (triangles), and E_{44}^S (squares), respectively. The family numbers $2n+m$ are shown for some cases.

and E_{44}^S consists of contributions from both the ETB single particle energy and from the many-body energy. This situation is clearly different from that for E_{11}^S and E_{22}^S for which there is a negligibly small family pattern in $\Sigma - E_{\text{bd}}$ and thus the family spread for E_{11}^S and E_{22}^S can be understood by the curvature effect.¹³ Within a $(2n+m)$ family, a SWNT with a chiral angle close to that of a zigzag nanotube gives a large spread value. Thus trigonal warping effect is responsible for both family spread in single particle energies, and for family spread in the many-body contributions.

The main reason for the chiral angle dependence of the many body effect is the chiral angle dependence of the effective mass of an electron and a hole. Since the effective mass has a strong type and chirality dependence because of the trigonal warping effect,²⁶ the Coulomb energy is modified by variations in the effective mass.

In Fig. 9, we plot the effective mass of the electron (left) and the hole (right) at the energy bottom (or top) for E_{11}^S (open circles), E_{22}^S (crosses), E_{33}^S (open triangles), and E_{44}^S (solid squares). Red and blue color shows type-I and -II

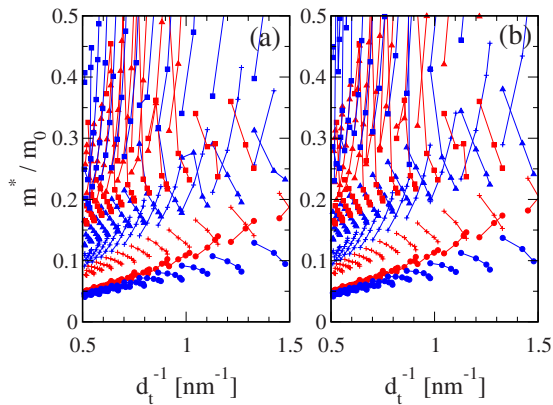


FIG. 9. (Color online) Effective mass of (a) an electron and (b) a hole as a function of d_t^{-1} . The red (blue) symbols denote semiconducting type I (type II), SWNTs, in which circles, pluses, triangles, and squares are for E_{11}^S (circles), E_{22}^S (pluses), E_{33}^S (triangles), and E_{44}^S (squares), respectively.

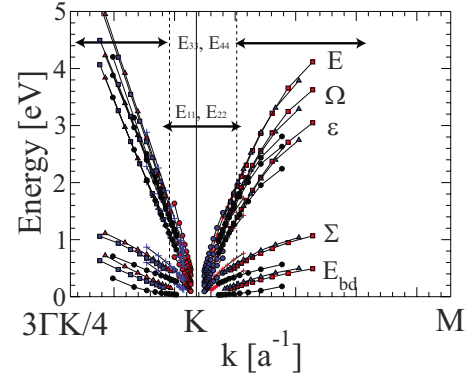


FIG. 10. (Color online) Quasiparticle energy E , exciton energy Ω , single particle energy ϵ , self-energy Σ , and binding energy E_{bd} of zigzag nanotubes are plotted as a function of wave vector k along the ΓKM line as we move along from the K point. Each of the following symbols denote E_{11} (circle), E_{22} (plus), E_{33} (triangle), and E_{44} (square). Red, blue, and black symbols denote semiconducting type I, type II, and metallic nanotubes, respectively. The arrows show that E_{ii} exist in the indicated regions.

tubes, respectively. The effective mass increases with increasing i in E_{ii}^S and shows a type and family behavior which is understood in terms of the trigonal warping effect.⁹ However, in the case of E_{33}^S and E_{44}^S , the effective masses appear in the same region, since the trigonal warping effect becomes large for large energies. This is the reason that $\Sigma - E_{\text{bd}}$ for E_{33}^S is similar to that for E_{44}^S . In the case of a hydrogen atom, the electron energy is proportional to the reduced mass, while in the case of the exciton of SWNTs, the energy is scaled as $m^{0.4}$.⁷ In the case of SWNTs, a larger E_{ii} energy generally gives a larger m , and thus we get a larger Coulomb energy.

This situation can be understood by Fig. 10. In Fig. 10, the single particle energy ϵ , the self-energy Σ , the quasiparticle energy $E \equiv \epsilon + \Sigma$, the exciton binding energy E_{bd} , and the exciton energy $\Omega \equiv E - E_{\text{bd}}$ of zigzag nanotubes are plotted as a function of wave vector k_{ii} along the ΓKM line of the 2D Brillouin zone of graphite. Each symbol is defined as E_{11} (circle), E_{22} (plus), E_{33} (triangle), and E_{44} (square). Red, blue, and black symbols denote semiconducting type-I, type-II, and metallic nanotubes, respectively. An important fact shown in Fig. 10 is that the self-energy Σ is larger than the exciton binding energy and that the difference between Σ and E_{bd} increases with increasing distance from the K point (or with both increasing the energy, or with decreasing the diameter). Thus the cancellation of the chiral angle dependence of the many-body effect between Σ and E_{bd} does not occur for E_{33}^S and E_{44}^S .

Both lines show that for E_{33}^S and E_{44}^S the self-energy is larger (0.2 eV for E_{11}^S and E_{22}^S and 0.5 eV for E_{33}^S and E_{44}^S , see also Fig. 9) than the exciton binding energy. This situation can be understood simply in terms of the effective masses of an electron and a hole. As we know for the hydrogen atom, the electronic states of a hydrogen atom can be expressed in terms of the Rydberg energy $me^4/2\hbar^2$. Thus the energy for a hydrogen atom is proportional to the reduced mass for an electron and proton. In the case of the exciton binding energy, the reduced mass for a photoexcited electron

at the conduction band bottom and a hole at the valence energy band top should be proportional to the binding energy. In the case of the self-energy, on the other hand, the reduced mass of a photoexcited electron and of an electron which lies near the valence band top should be considered. Since the effective mass of the valence electrons increases with increasing distance k (or with decreasing energy) from the valence band top, the averaged reduced mass for the self-energy is always larger than that for the exciton. This is a simple explanation why the self-energy is larger than the exciton binding energy.

IV. SUMMARY

In summary, we show that the higher exciton states E_{33}^S and E_{44}^S have a large chirality dependence for many body effects. Thus the treatment that the chirality dependence of E_{ii} comes only from a single particle energy works only for the E_{11}^S and E_{22}^S excitonic states. For E_{11}^M , although the many-

body effects do not show a family spread, the diameter dependence of the many-body effect deviates from the logarithmic function.

For the higher E_{ii}^S transitions, we see a crossing of the family pattern with nearest E_{jj}^S family patterns. We suggest that E_{ii}^S should be defined along smooth family pattern lines. A discontinuity in k_{ii}^S at the E_{ii}^S crossing points is thus expected. In order to check the calculated results by experiments, G' band Raman measurements will be desired, since the G' band frequency depends on the wave vector of phonons due to double resonance Raman theory.²⁸

ACKNOWLEDGMENTS

R.S. thanks J. L. Sauvajol for giving us the experimental data for E_{ii} . R.S. acknowledges a Grant-in-Aid (No. 16076201) from the Ministry of Education, Japan. MIT authors acknowledge support under NSF Grants No. DMR 04-05538.

- ¹C. D. Spataru, S. Ismail-Beigi, L. X. Benedict, and S. G. Louie, *Phys. Rev. Lett.* **92**, 077402 (2004).
- ²C. D. Spataru, S. Ismail-Beigi, R. B. Capaz, and S. G. Louie, *Phys. Rev. Lett.* **95**, 247402 (2005).
- ³F. Wang, G. Dukovic, L. E. Brus, and T. F. Heinz, *Science* **308**, 838 (2005).
- ⁴J. Maultzsch, R. Pomraenke, S. Reich, E. Chang, D. Prezzi, A. Ruini, E. Molinari, M. S. Strano, C. Thomsen, and C. Lienau, *Phys. Rev. B* **72**, 241402(R) (2005).
- ⁵T. Ando, *J. Phys. Soc. Jpn.* **66**, 1066 (1997).
- ⁶E. Chang, G. Bussi, A. Ruini, and E. Molinari, *Phys. Rev. Lett.* **92**, 196401 (2004).
- ⁷V. Perebeinos, J. Tersoff, and Ph. Avouris, *Phys. Rev. Lett.* **92**, 257402 (2004).
- ⁸V. Perebeinos, J. Tersoff, and Ph. Avouris, *Phys. Rev. Lett.* **94**, 027402 (2005).
- ⁹R. Saito, G. Dresselhaus, and M. S. Dresselhaus, *Phys. Rev. B* **61**, 2981 (2000).
- ¹⁰Ge. G. Samsonidze, R. Saito, A. Jorio, M. A. Pimenta, A. G. Souza Filho, A. Grüneis, G. Dresselhaus, and M. S. Dresselhaus, *J. Nanosci. Nanotechnol.* **3**, 431 (2003).
- ¹¹R. Saito, K. Sato, Y. Oyama, J. Jiang, Ge. G. Samsonidze, G. Dresselhaus, and M. S. Dresselhaus, *Phys. Rev. B* **72**, 153413 (2005).
- ¹²R. Saito, G. Dresselhaus, and M. S. Dresselhaus, *Physical Properties of Carbon Nanotubes* (Imperial College Press, London, 1998).
- ¹³Ge. G. Samsonidze, R. Saito, N. Kobayashi, A. Grüneis, J. Jiang, A. Jorio, S. G. Chou, G. Dresselhaus, and M. S. Dresselhaus, *Appl. Phys. Lett.* **85**, 5703 (2004).
- ¹⁴C. Fantini, A. Jorio, M. Souza, R. Saito, Ge. G. Samsonidze, M. S. Dresselhaus, and M. A. Pimenta, *Phys. Rev. B* **72**, 085446 (2005).
- ¹⁵R. Saito, M. Fujita, G. Dresselhaus, and M. S. Dresselhaus, *Appl. Phys. Lett.* **60**, 2204 (1992).
- ¹⁶Y. Ohno, S. Iwasaki, Y. Murakami, S. Kishimoto, S. Maruyama, and Takashi Mizutani, *Phys. Rev. B* **73**, 235427 (2006).
- ¹⁷M. S. Dresselhaus, G. Dresselhaus, R. Saito, and A. Jorio, *Phys. Rep.* **409**, 47 (2005).
- ¹⁸M. S. Dresselhaus, G. Dresselhaus, R. Saito, and A. Jorio, in *Annual Reviews of Physical Chemistry Chemical Physics*, edited by Maria Duncan (Intelligent Synthesis of the Scientific Literature, Palo Alto, CA, 2007).
- ¹⁹Y. Miyauchi, R. Saito, K. Sato, Y. Ohno, S. Iwasaki, T. Mizutani, J. Jiang, and S. Maruyama, *Chem. Phys. Lett.* **442**, 394 (2007).
- ²⁰V. N. Popov, *New J. Phys.* **6**, 17 (2004).
- ²¹C. L. Kane and E. J. Mele, *Phys. Rev. Lett.* **93**, 197402 (2004).
- ²²A. Jorio, C. Fantini, M. A. Pimenta, R. B. Capaz, Ge. G. Samsonidze, G. Dresselhaus, M. S. Dresselhaus, J. Jiang, N. Kobayashi, A. Grüneis, and R. Saito, *Phys. Rev. B* **71**, 075401 (2005).
- ²³J. Jiang, R. Saito, Ge. G. Samsonidze, A. Jorio, S. G. Chou, G. Dresselhaus, and M. S. Dresselhaus, *Phys. Rev. B* **75**, 035407 (2007).
- ²⁴A. Jorio, P. T. Araujo, S. K. Doorn, S. Maruyama, H. Chacham, and M. A. Pimenta, *Phys. Status Solidi B* **243**, 3117 (2006).
- ²⁵P. T. Araujo, S. K. Doorn, S. Kilina, S. Tretiak, E. Einarsson, S. Maruyama, H. Chacham, M. A. Pimenta, and A. Jorio, *Phys. Rev. Lett.* **98**, 067401 (2007).
- ²⁶K. Sato, R. Saito, J. Jiang, G. Dresselhaus, and M. S. Dresselhaus, *Vib. Spectrosc.* (to be published).
- ²⁷J. Jiang, R. Saito, A. Grüneis, G. Dresselhaus, and M. S. Dresselhaus, *Carbon* **42**, 3169 (2004).
- ²⁸R. Saito, A. Jorio, A. G. Souza Filho, G. Dresselhaus, M. S. Dresselhaus, and M. A. Pimenta, *Phys. Rev. Lett.* **88**, 027401 (2001).
- ²⁹Ge. G. Samsonidze, R. Saito, A. Jorio, A. G. Souza Filho, A. Grüneis, M. A. Pimenta, G. Dresselhaus, and M. S. Dresselhaus, *Phys. Rev. Lett.* **90**, 027403 (2003).
- ³⁰T. Ando, *J. Phys. Soc. Jpn.* **75**, 024707 (2006).
- ³¹E. B. Barros, R. B. Capaz, A. Jorio, Ge. G. Samsonidze, A. G. Souza Filho, S. Ismail-Beigi, C. D. Spataru, S. G. Louie, G. Dresselhaus, and M. S. Dresselhaus, *Phys. Rev. B* **73**, 241406(R) (2006).
- ³²T. Michel, M. Paillet, J. C. Meyer, V. N. Popov, L. Henrard, and J.-L. Sauvajol, *Phys. Rev. B* **75**, 155432 (2007).
- ³³V. Zolyomi and J. Kurti, *Phys. Rev. B* **70**, 085403 (2004).